The formation of $FeCO_3$ and Fe_3O_4 on carbon steel and their protective capabilities against CO_2 corrosion at elevated temperature and pressure

Yong Hua[a]*, Shusheng Xu[a], Yun Wang[c], Wassim Taleb[a], Jianbo Sun[b], Lei Zhang[c], Richard Barker[a] and Anne Neville[a]
a: Institute of Functional Surfaces, School of Mechanical Engineering, University of Leeds, Leeds, LS2 9JT, United Kingdom.
b: School of Mechanical and Electronic Engineering, China University of Petroleum, Qingdao, Shandong, China.
c: Corrosion and Protection Centre, University of Science and Technology Beijing, 30 Xueyuan road, Beijing, China.

*Corresponding author: Yong Hua, Tel: +44 (0) 7923359918, fax: +44 (0) 1132424611.
Email: Y.Hua@leeds.ac.uk

Abstract

This study investigates the corrosion performance of X65 carbon steel at elevated temperatures (up to 250°C) and CO_2 partial pressures (up to 28.5 bar pCO_2). A detailed appraisal of how the corrosion products can protect against general and localised corrosion is presented. The morphology and chemical composition of corrosion products were determined using various microscopic and spectroscopic techniques, with localised corrosion rates being determined by surface profilometry. An increase in temperature or reduction in CO_2 partial pressure favours the formation of a protective magnetite layer. It is thermodynamically more stable and more protective than iron carbonate in these conditions.

Keywords: Fe_3O_4, $FeCO_3$, CO_2 corrosion, carbon steel

1.0 Introduction

Carbon dioxide (CO_2) corrosion of carbon steel pipelines is a common occurrence in the oil and gas industry. The CO_2 corrosion mechanism has recently received renewed interest, resulting in an improved understanding of the anodic and cathodic reaction pathways at low temperatures (<90°C) [1, 2, 3]. Despite the CO_2 corrosion mechanism below 90°C being widely investigated, the electrochemical reactions and formation of corrosion products beyond 90°C have received significantly less attention.

When carbon steel is exposed to CO_2 environments, the main anodic reaction which occurs is the dissolution of iron:

$$Fe_{(s)} \rightarrow Fe^{2+}_{(aq)} + 2e^- \quad (1)$$

The corresponding cathodic reactions below 90°C have been confirmed to be hydrogen evolution from a combination of H^+, H_2CO_3, HCO_3^- and H_2O reduction (noting that H_2CO_3 and HCO_3^- contribute to the cathodic reaction via a 'buffering effect' whereby they dissociate at the steel surface, producing the H^+ ions which subsequently undergo hydrogen-evolution):

$$2H^+_{(aq)} + 2e^- \rightarrow H_{2(g)} \quad (2a)$$

$$2H_2CO_{3(aq)} + 2e^- \rightarrow H_{2(g)} + 2HCO^-_{3(aq)} \quad (2b)$$

$$2HCO^-_{3(aq)} + 2e^- \rightarrow H_{2(g)} + 2CO^-_{3(aq)} \quad (2c)$$

$$2H_2O_{(l)} + 2e^- \rightarrow H_{2(g)} + 2OH^-_{(aq)} \quad (2d)$$

The formation of corrosion products is normally a key process in the CO_2 corrosion mechanism and their presence can significantly alter the rate and mechanism of corrosion. The corrosion products capable of forming on carbon steel vary depending upon the exposed environment and operating conditions, affording different levels of protection to the steel substrate depending upon their formation kinetics, chemistry and morphology [4, 5, 6, 7, 8]. Failure to account for the presence of such products can result in over-prediction of the corrosion severity and a high degree of conservatism being integrated into CO_2 corrosion prediction models.

Research indicates that the most common corrosion product to form on carbon steel is iron carbonate ($FeCO_3$) at temperatures up to 90°C in CO_2 environments [9, 10, 11, 12]. When carbon steel is exposed to CO_2-saturated solutions, Fe^{2+} ions can accumulate within the process fluid. Once the product of the activities of Fe^{2+} and CO_3^{2-} ions reach and exceed a particular saturation limit, $FeCO_3$ can precipitate via Equation (3):

$$Fe^{2+}_{(aq)} + CO^{2-}_{3(aq)} \rightarrow FeCO_{3(s)} \quad (3)$$

A $FeCO_3$ layer can reduce the corrosion rate by over one order of magnitude in some instances[4, 11, 13]. The formation of such a layer can block active sites on the steel surface and restrict the transport of electrochemically-active species [8, 10, 11, 13, 14]. Authors have

also reported that $FeCO_3$ films can adopt a double-layer structure under specific conditions, consisting of an outer crystalline layer and an inner amorphous or nano-crystalline film. In this instance, the protection afforded to the substrate has been suggested to arise predominantly from the inner layer[10, 15].

In addition to the formation of $FeCO_3$, a number of additional corrosion products have been reported at temperatures below 90°C, some of which include iron hydroxide ($Fe(OH)_2$), chukanovite ($Fe_2(OH)_2CO_3$) and magnetite (Fe_3O_4)[16, 17, 18, 19]. Towards higher pH and higher temperature, researchers tend to report the dominance of either $FeCO_3$, $Fe_2(OH)_2CO_3$ or Fe_3O_4[15, 16, 18, 19, 20].

From literature, it is evident that transitions to different corrosion products occur as temperature is increased, owing to a change in the thermodynamic stability of different compounds. At low temperature (<60°C), the steel surface is typically free from corrosion products, except in specific circumstances where solution pH is high or the solution is highly supersaturated with respect to corrosion products at the steel-electrolyte interface for prolonged periods[9, 19, 21].

As the operating temperature exceeds 60°C, numerous authors have reported corrosion rates declining with increasing temperature, with dissolution rate typically peaking in the range 60 to 120°C, depending upon the exact operating conditions [4, 11, 16, 21, 22]. Critical factors influencing the sensitivity of the location of the corrosion peak include CO_2 partial pressure[11, 16, 22], pH[23, 24], water chemistry and flow characteristics [25, 26]. Typically, only $FeCO_3$ can be observed on the surface of carbon steel immersed in a NaCl solution saturated with CO_2 at temperatures of around 80°C. However, as temperatures rises beyond this temperature, authors have reported both changes in the appearance of the $FeCO_3$ layer (in terms of thickness and grain sizes), as well as transitions in the surface species formed, with Fe_3O_4 being commonly reported. As an example, Shannon[27] evaluated the formation of corrosion products in geothermal brines. At a pH of 4.8, no corrosion products were observed at 50°C, whilst $FeCO_3$ was recorded at 150°C. Further increase of temperature to 250°C resulted in a corrosion product comprising of 70% Fe_3O_4 and 30% $FeCO_3$. Increasing pH to 7.5 resulted in Fe_3O_4 forming at both 150 and 250°C, suggesting that increased pH and temperature favour the formation of Fe_3O_4.

In another study, Yin et al.[20] reported a change in corrosion product structure in their experiments, with finer $FeCO_3$ crystals and thinner layers being associated with superior

corrosion protection as temperature was increased from 50 to 180°C for carbon steel exposed to CO_2 environments. Again, above 100°C, the onset of trace amounts of Fe_3O_4 formation was reported in conjunction with $FeCO_3$. This observation was supported by the findings of Han et al.[17] who utilised grazing incidence XRD and TEM to study the protective layers formed on carbon steel at pH 8 and 80°C in a CO_2-saturated NaCl brine solution. Their results showed that $FeCO_3$ was able to form under such conditions, however, the high local pH within the film created a favourable environment for the formation of Fe_3O_4 at the boundaries between $FeCO_3$ and the steel substrate.

Tanupabringsen et al.[18] constructed Pourbaix diagrams for an Fe-CO_2-H_2O system at elevated temperatures using thermodynamic theory. The diagrams were correlated with the observed corrosion products on carbon steel up to 250°C through consideration of surface pH within each experiment. For the 4 day experiments performed between 80 and 150°C, $FeCO_3$ and $Fe_2(OH)_2CO_3$ were observed as the dominant corrosion products, with corrosion rate peaking at 120°C, whereas Fe_3O_4 was detected at 200 and 250°C. Variation of exposure time showed that $Fe_2(OH)_2CO_3$ ultimately transformed into $FeCO_3$, consistent with the calculated relative thermodynamic stability of each compound.

Supplementary experiments were performed by Tanupabringsen et al.[24] in another study over 20 hours to evaluate the susceptibility of carbon steel to corrosion at temperatures of 80°C, 120°C, 150°C and 200°C. In these experiments the pH and dissolved CO_2 was controlled at 0.030M to determine the isolated effect of temperature. Their findings indicated that the corrosion rates reduced with increasing temperature and that the corrosion product was exclusively $FeCO_3$ below 150°C, but comprised of $FeCO_3$ and Fe_3O_4 when the temperature reached 150°C.

Despite the recent research into the CO_2 corrosion mechanism at elevated temperatures, there still remains some questions regarding the preferential formation of the surface products and their controlling factors. In addition, the formation of Fe_3O_4 and the extent to which it protects carbon steel from localised attack has not been thoroughly investigated.

This current study is conducted over a wide temperature range of 90°C to 250°C in an effort to determine the role of simultaneous increases in temperature, CO_2 partial pressure and pH on the corrosion products and how these relate to general and localised

corrosion behaviour. Furthermore, studies are performed to isolate the effects of temperature and CO_2 partial pressure on $FeCO_3$ and Fe_3O_4 formation.

In the first series of the experiments, the starting pressure and pH in the autoclave are allowed to evolve naturally with temperature (achieved by shutting in the system at room temperature and pressure before heating). In the second series of tests, the pH, CO_2 partial pressure and temperature are all controlled to isolate the individual effects of CO_2 partial pressure and temperature, and draw conclusions regarding the role of each parameter.

2.0 Experimental procedure

2.1 Material and Methods

The chemical composition of carbon steel (API 5L X65) used in this study is provided in Table 1. The mass loss samples were machined into discs of 25mm diameter and thickness of 5 mm. The steel sample surfaces were wet-ground up to 600 grit SiC paper, followed by rinsing with distilled water, ethanol and drying with compressed air. Samples were weighed immediately using an electronic balance (within an accuracy of 0.01 mg). Two samples (27 cm^2) were exposed to a 650 ml solution within a one litre capacity autoclave in each experiment.

Table 1: Elemental composition of X65 steel (wt.%)

C	**P**	**Si**	**Cr**	**Mn**	**Ni**	**S**	**Mo**
0.12	0.008	0.18	0.11	1.27	0.07	0.002	0.17
Cu	**B**	**Sn**	**Ti**	**Al**	**Fe**	**Nb**	**V**
0.12	0.0005	0.008	0.001	0.022	Balance	0.054	0.057

Figure 1 shows a schematic representation of the autoclave setup. The brine used in all experiments was de-aerated by continuously purging with CO_2 for a minimum of 12 hours. Two samples were placed on a Polyether ether ketone (PEEK) sample holder within the autoclave. Before transferring the test solution into the autoclave, all the lines were flushed out using high pressure CO_2. The prepared CO_2-saturated brine was then carefully delivered into the autoclave, followed by pressurising to a specific CO_2 partial pressure at 25°C before heating to the required test temperature. The various test

conditions evaluated within this study are provided in Table 2 and Table 3. The initial solution pH at elevated temperatures and CO_2 partial pressures were predicted using MultiScale software[28] and are also provided in Table 2 and Table 3.

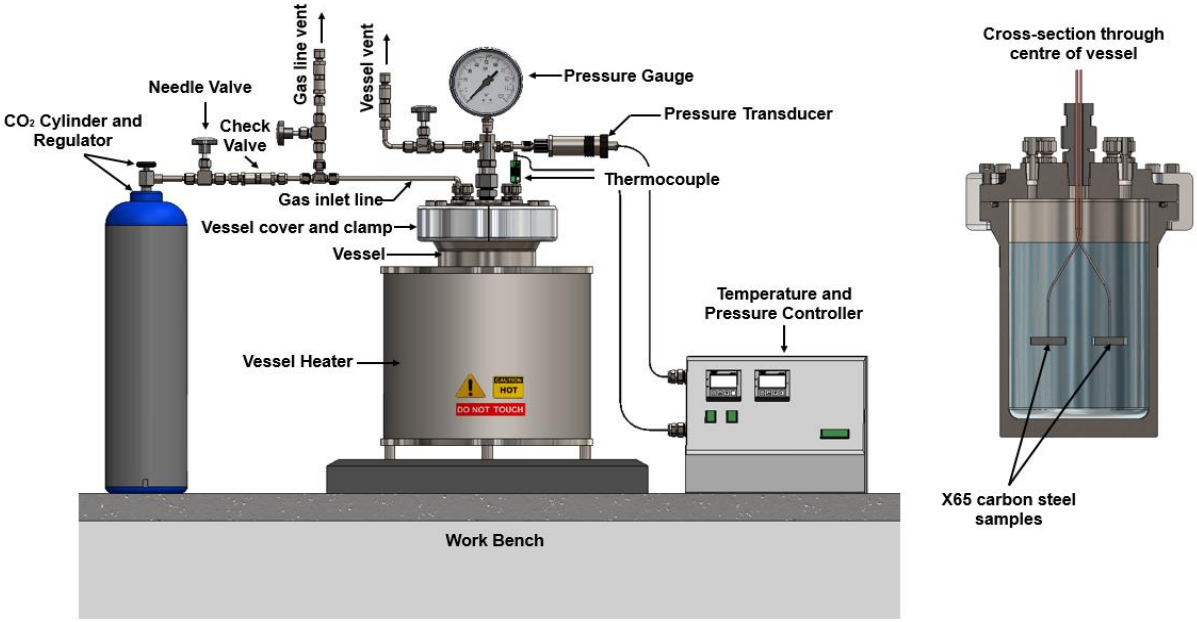

Figure 1: Schematic of autoclave setup

Table 2: Test matrix for corrosion tests for samples exposed to various temperatures

Brine composition, mg/L	Temp, °C	Measured CO_2 pressure at 25°C, bar	Predicted pH at elevated temperature	CO_2 partial pressure, bar	Total pressure, bar	Immersion time, hours
NaCl solution, Cl^-: 29503, $NaHCO_3$: 585, pH: 5.6	90	10	4.9	13.3	14	48
	150		5.3	14.3	19	
	200		5.7	15.4	31	
	250		6.3	15.4	55	

Table 3: Test matrix for corrosion tests under various CO_2 partial pressure

Brine composition, mg/L	Temp, °C	Measured CO_2 pressure at 25°C, bar	Predicted pH at 200 °C	CO_2 partial pressure, bar	Total pressure, bar	Immersion time, hours
NaCl solution,		1	6.4	2.7	18	48
		3	6.1	6.5	22	

Cl^-: 29503, $NaHCO_3$: 585, pH: 5.6	200	10	5.7	15.4	31	
		20	5.4	28.5	44	

159

160 Upon completion of each test, the samples were removed from the autoclave, cleaned
161 with distilled water and dried thoroughly. In accordance with ASTM Standard G1-03[29],
162 the corrosion products on the surface were removed with Clarke's solution, followed by
163 rinsing with distilled water and ethanol before drying with compressed air.

164 The corrosion rates were calculated by using Equation (4):

$$V_c = \frac{87600\Delta m}{\rho A T} \quad (4)$$

165 where V_C is the corrosion rate of the sample in mm/y, Δm is the mass loss in grams, ρ is
166 the density of the sample in g/cm^3, A is the exposed area in cm^2 and T is the immersion
167 time in hours.

168 ***2.2 Surface analysis***

169 All SEM images were acquired using a Carl Zeiss EVO MA15 scanning electron microscope
170 (SEM). A 20 keV accelerating voltage and 8 mm working distance were used for all images.

171 The crystalline nature of corrosion products was determined using X-ray diffraction (XRD)
172 (D8 advance, Bruker) and obtained by employing Cu Kα radiation over a scattering angle
173 range of 2Θ=10 to 70°. The step size was 0.033 per second and approximately 49 minutes
174 were required per scan.

175 Raman spectroscopy was used to identify potential amorphous corrosion products
176 formed on the surface which XRD would be unable to detect. An Ar ion laser with low
177 intensity power (less than 1%) was used and approximately 40 minutes was required for
178 each scan point.

179 ***2.3 Focused ion beam scanning electron microscopy and transmission electron***
180 ***microscopy***

181 The corrosion product formed at the material interface in specific experiments was
182 sectioned using a focused ion beam scanning electron microscope (FIB-SEM) and
183 analysed further using transmission electron microscopy (TEM). More details relating to

184 the techniques applied and the microscope operating parameters can be found in a
185 previous publication.[6]

186 ### *2.4 Non-contact interferometry*

187 To quantify the localised attack on the carbon steel samples, an NP_{FLEX} 3D Surface
188 Metrology System was used. The corrosion products formed on the surface were first
189 removed by using Clarke's solution. Localised corrosion was the quantified through the
190 implementation of ASTM Standard G46-94.[30]

191 ## *3.0 Results*

192 ### *3.1 General corrosion behaviour of X65 with increasing temperature*

193 Figure 2 presents the corrosion rates and corrosion product mass of X65 carbon steel
194 exposed to CO_2-saturated 4.9 wt.% NaCl solution for 48 hours at elevated temperatures.
195 The results show that X65 has highest corrosion rate of 3.19 mm/year at the lowest
196 temperature of 90°C. General corrosion rates of 0.57, 0.36 and 0.38 mm/year are
197 recorded for temperatures of 150°C, 200°C and 250°C, respectively over 48 hours of
198 exposure. The general corrosion rate decreases with increasing temperature, with nearly
199 an order of magnitude reduction being recorded by increasing temperature from 90 to
200 200°C. Interestingly, the corrosion product mass reduces in conjunction with the
201 corrosion rate, signifying that the lowest corrosion rate is associated with the lowest
202 corrosion product mass. The results suggest that with increasing temperature, protective
203 film formation is accelerated. The analysis of corrosion product morphology and
204 composition are described in the following sections.

205

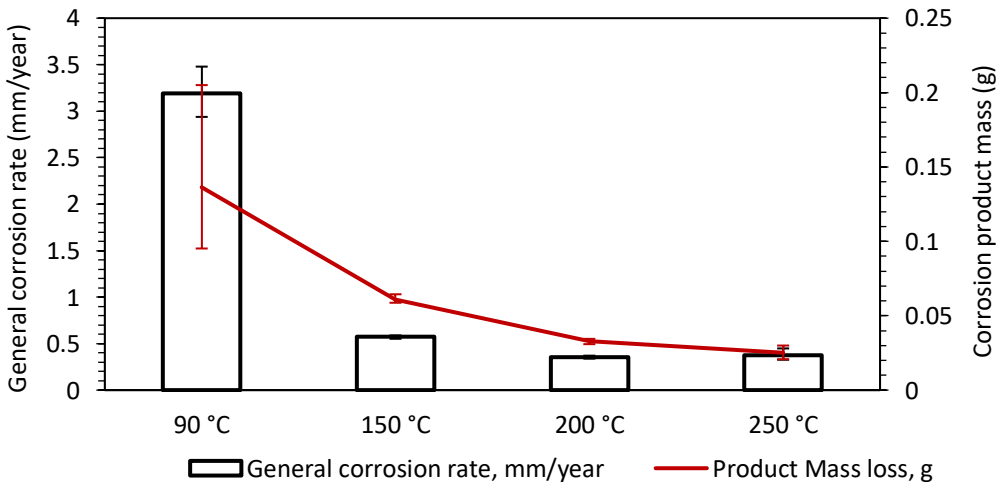

206

Figure 2: Average general corrosion rates of X65 carbon steel over 48 hours of exposure to a CO_2-saturated 4.9 wt.% NaCl solution as a function of temperature. Exact test conditions at each temperature are outlined in Table 2.

3.2 Analysis of corrosion product morphology and composition

The reduction in X65 general corrosion rate in conjunction with increased temperature (Figure 2) suggests that protective film formation plays a critical role in the CO_2 corrosion mechanism. Figure 3 shows SEM images of the steel surface after 48 hours of exposure to each test temperature evaluated in Figure 2. After 48 hours, a dense and compact corrosion product layer appears on the steel surface at temperatures of 90°C and 150°C (Figure 3(a) and (b)) which cover the entire steel surface. As the temperature is increased to 200°C, gaps between the crystals become evident and their coverage reduces. At 250°C, crystals are randomly distributed on the steel surface and become fewer in number. Perhaps intuitively, it may be expected from analysis of the SEM images that the corrosion product formed at 250°C would be the least protective. However, the reality is on the contrary, with the substrate having the lowest coverage of crystals possessing the lowest general corrosion rate over the duration of the experiment.

XRD was employed to determine the crystal structure of the various corrosion products formed on each steel surface and the corresponding diffraction patterns are shown in Figure 4. The patterns show that the dominant crystalline phase detected on all steel surfaces is $FeCO_3$, which relates to the large, cubic crystals clearly visible at temperatures of 90°C, 150°C and 200°C. Traces of Fe_3O_4 coexisting within the $FeCO_3$ corrosion product were also detected at a temperature of 250°C. It is possible that Fe_3O_4 exists on the steel surface at 200°C, however, its amount is below the detection limit of XRD. The lower corrosion rates at higher temperature, and the gradual transition from $FeCO_3$ to Fe_3O_4 suggests that the Fe_3O_4 layer offers superior corrosion protection compared to $FeCO_3$. In addition, the increase in temperature up to 250°C resulted in Fe_3O_4 becoming the more stable corrosion product compared to $FeCO_3$ under these conditions.

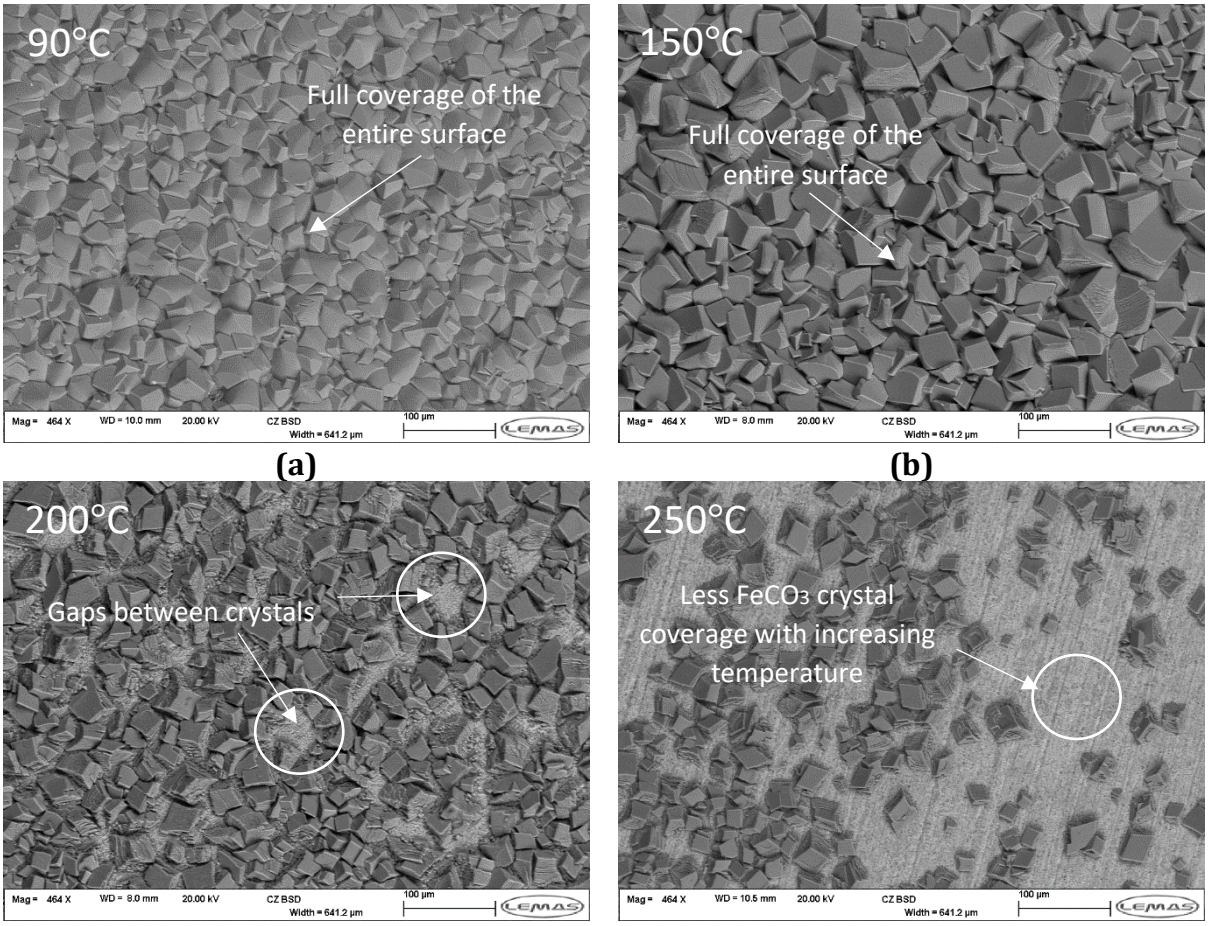

Figure 3: SEM images of the corrosion products formed on X65 carbon steel surfaces after 48 hour exposure to a CO_2-saturated 4.9 wt.% NaCl brine at temperatures of (a) 90°C, (b) 150°C, (c) 200°C and (d) 250°C. Exact test conditions at each temperature are outlined in Table 2.

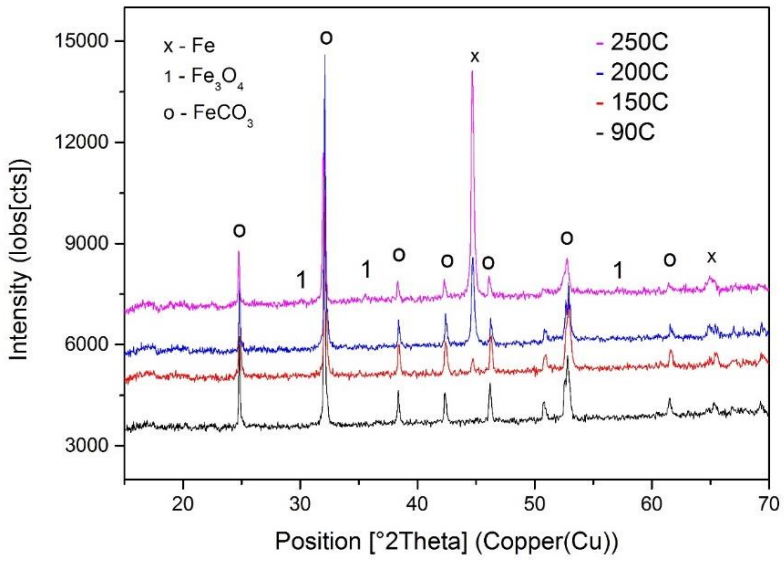

Figure 4: XRD patterns of the corrosion products formed on X65 steel surfaces after 48 hour exposure to a CO_2-saturated 4.9 wt.% NaCl brine at temperatures

ranging from 90 to 250°C. Exact test conditions at each temperature are outlined in Table 2.

3.3 The influence of CO_2 partial pressure on the general corrosion rates of X65 at 200°C

The effect of CO_2 partial pressure on the corrosion behaviour of X65 carbon steel at a fixed temperature of 200°C was evaluated, with the substrate mass loss and corrosion product mass results provided in Figure 5.

Figure 5 shows that the general corrosion rate increased as CO_2 partial pressure increased. The lowest corrosion rate of 0.17 mm/year was recorded at 200°C and 2.7 bar of CO_2 partial pressure. A general corrosion rate of 0.41 mm/year was recorded when CO_2 partial pressure increased to 28.5 bar at the same temperature of 200°C. This effect can at least partly be attributed to the reduction in pH achieved with increasing CO_2 partial pressure, which increases the corrosivity of the test solution by increasing the H^+ concentration, which is able to support the cathodic hydrogen evolution reaction.

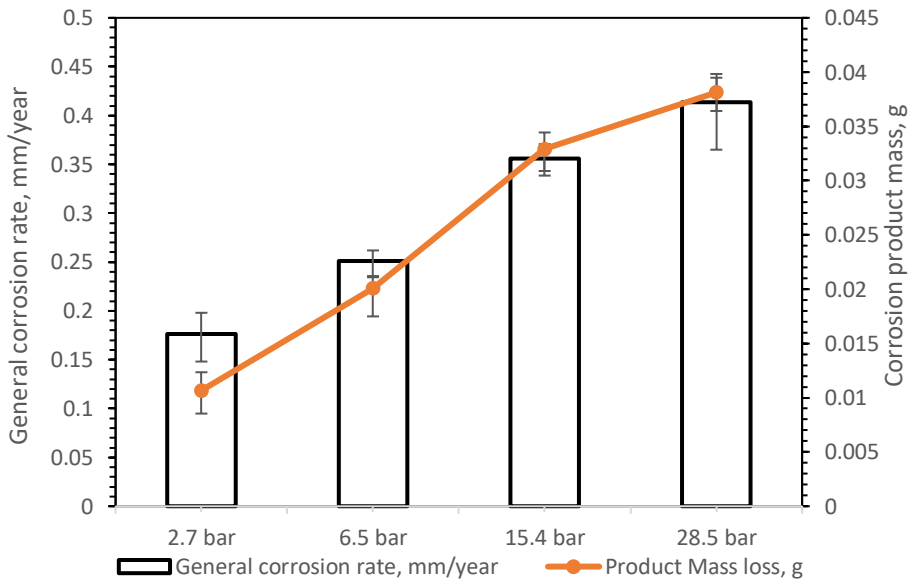

Figure 5: Average general corrosion rates of X65 carbon steel over 48 hours of exposure to a CO_2-saturated 4.9 wt.% NaCl solution at 200°C as a function of CO_2 partial pressure. Exact test conditions at each temperature are outlined in Table 3.

3.4 Analysis of corrosion product morphology and their compositions

SEM images for X65 exposed to different CO_2 partial pressures at a fixed temperature of 200°C and immersion time of 48 hours are shown in Figure 6. Traces of crystalline

corrosion products (confirmed as $FeCO_3$ from XRD patterns in Figure 7) can be observed at 2.7 bar CO_2 partial pressure, as shown in Figure 6(a), in conjunction with Fe_3O_4, also determined from XRD analysis in Figure 7. Increasing CO_2 partial pressure to 6.5 bar (Figure 6(b)) resulted in a greater quantity of $FeCO_3$ forming on the steel surface. Gaps between the precipitated crystals are still evident as the CO_2 partial pressure is increased to 15.4 bar (Figure 6(c)). However, a dense and compact $FeCO_3$ layer forms on the steel surface at a CO_2 partial pressure of 28.5 bar (Figure 6(d)). The images reveal that increasing CO_2 partial pressure has the opposite effect on the formation of $FeCO_3$ compared to increasing temperature i.e. reduced CO_2 partial pressure and increased temperature both supress the formation of $FeCO_3$ and favour the formation of Fe_3O_4.

The XRD patterns for the samples exposed to various CO_2 partial pressure for a fixed temperature of 200°C (Figure 7) indicated that the crystalline phases were $FeCO_3$ and Fe_3O_4 at 2.7 and 6.5 bar CO_2 partial pressure. Larger crystals which are clearly visible on the X65 steel at 15.4 and 28.5 bar of CO_2 partial pressure were determined to be $FeCO_3$ according to the XRD analysis in Figure 7. It was not clear whether Fe_3O_4 coexisted within the corrosion products at these two higher pressures.

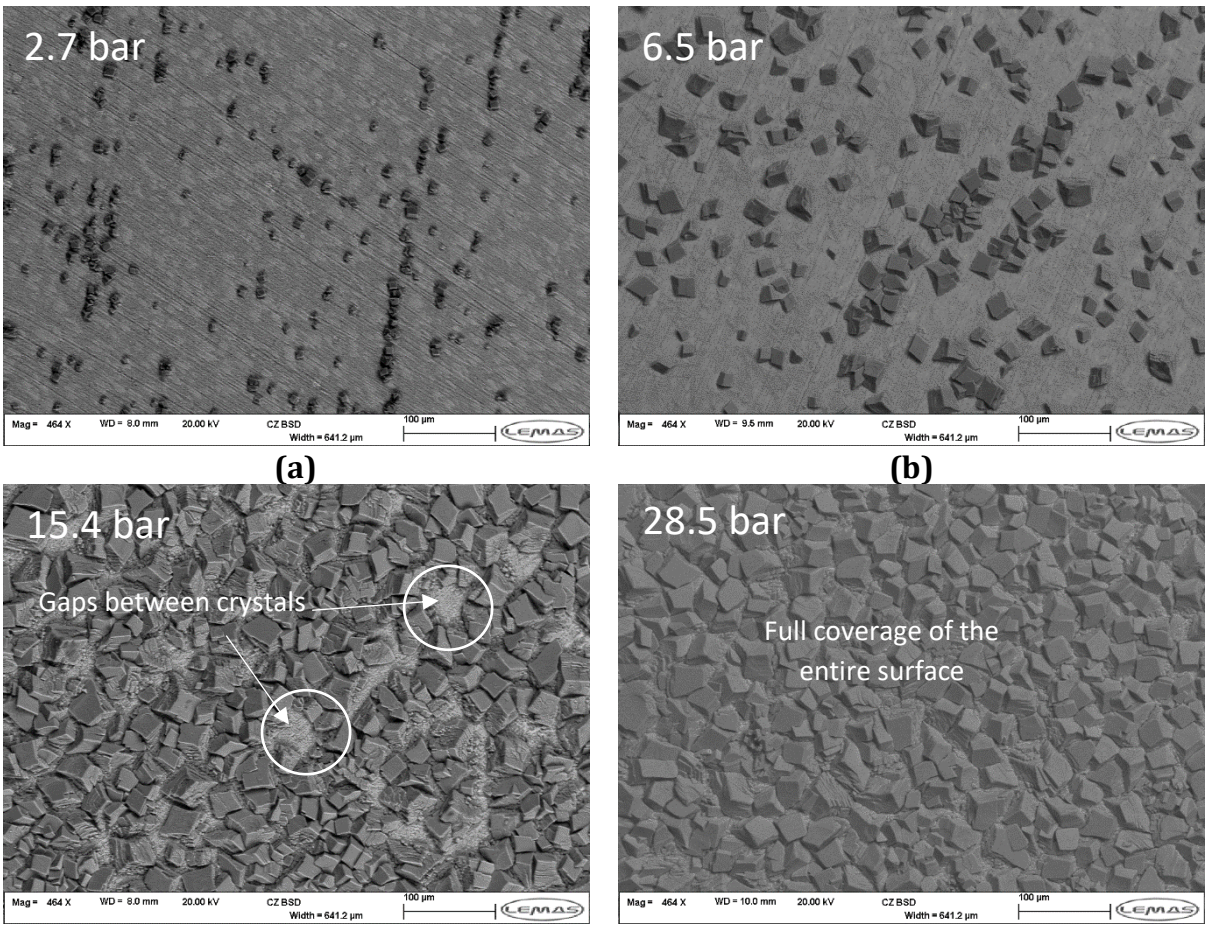

(c) **(d)**

Figure 6: SEM images of the corrosion products formed on X65 carbon steel surfaces after 48 hour exposure to a CO_2-saturated 4.9 wt.% NaCl brine at 200°C and CO_2 partial pressures of (a) 2.7 bar, (b) 6.5 bar, (c) 15.4 bar and (d) 28.5 bar. Exact test conditions at each temperature are outlined in Table 3.

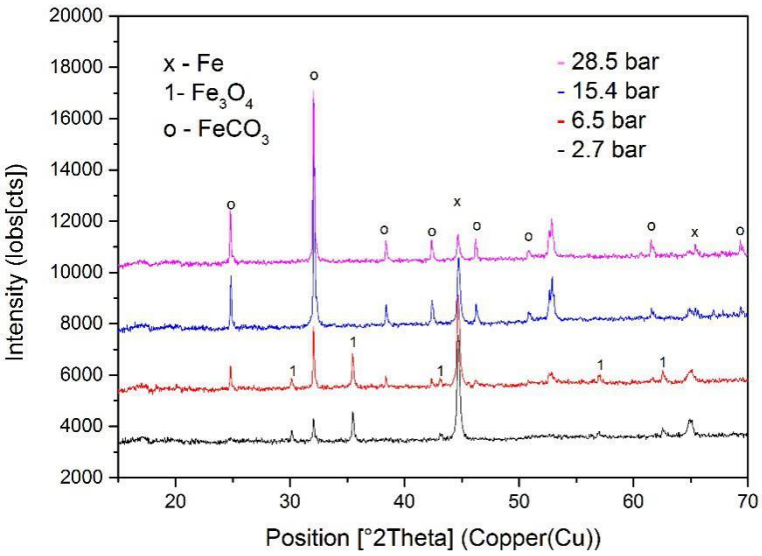

Figure 7: XRD patterns of the corrosion products formed on X65 carbon steel surfaces after 48 hour exposure to a CO_2-saturated 4.9 wt.% NaCl brine at 200°C and different CO_2 partial pressures. Exact test conditions at each temperature are outlined in Table 3.

3.5 Localised corrosion assessment

One particular concern in such severe high temperature and high pressure environments is the occurrence of localised/pitting corrosion. Figure 8 provides a comparison between the general and localised corrosion behaviour of carbon steel across all test conditions outlined in Tables 2 and 3. Figure 9 shows the morphologies of the localised/pitting attack at various temperatures and CO_2 partial pressures.

The localised corrosion rates shown in Figure 8 produce a similar trend with increasing temperature and pressure to the general corrosion rates presented in the same figure. From Figure 8(a), the localised corrosion rate was found to reduce with increasing temperature from 9.2 mm/year to 0.9 mm/year as temperature was increased from 90 to 250°C. Furthermore, it is interesting to note that the sizes and depths of the localised/pitted regions decreased as temperature was increased from 90°C to 250°C, as shown in Figure 9(a) and 9(b).

Figure 8(b) indicates that as CO_2 partial pressure was increased at a constant temperature of 200°C, the extent of localised corrosion increased with the general corrosion behaviour, with localised material loss rates increasing from 0.74 to 3.7 mm/year as CO_2 partial pressure was increased from 2.7 to 28.5 bar. Large regions of localised attack can be observed after removal of the corrosion products on the surface as shown in Figure 9(c) and 9(d).

In all the tests performed, the localised corrosion rates are approximately two or three times higher than the general corrosion rates over this particular period of time. It is important to stress that these measurements provide an indication as to the extent of pitting/localised attack over 48 hours only and should not be extrapolated to long term behaviour without further analysis. Nonetheless, they provide a comparison of the severity of each environment over the initial stages of localised attack within 48 hours.

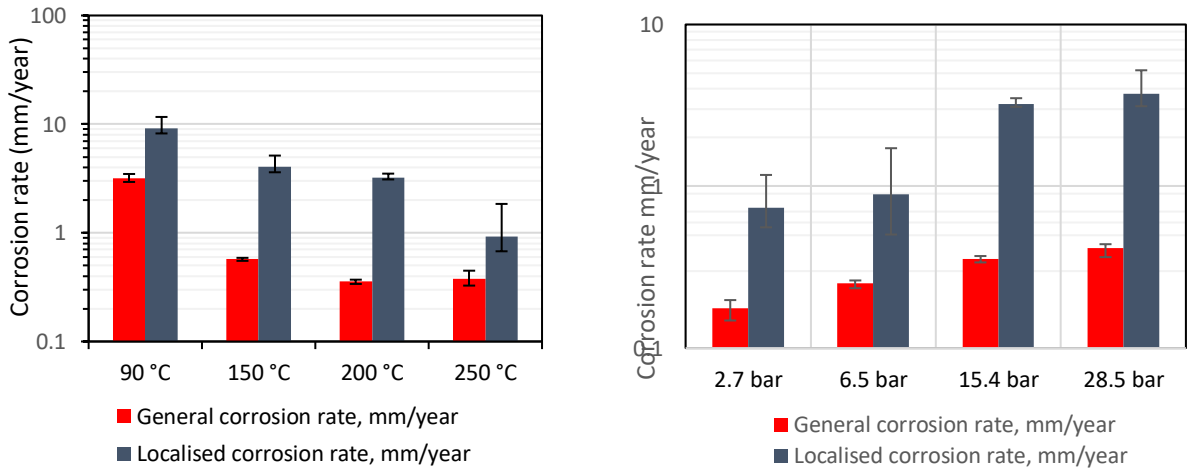

(a) **(b)**

Figure 8: Average general and localised corrosion rates of X65 carbon steel over 48 hour exposure to a CO_2-saturated 4.9 wt.% NaCl solution as a function of (a) temperature with CO_2 pressure ranges between 13.3 and 15.4 bar and (b) CO_2 partial pressure at a fixed temperature of 200°C. Exact test conditions at each temperature are outlined in Tables 2 and 3.

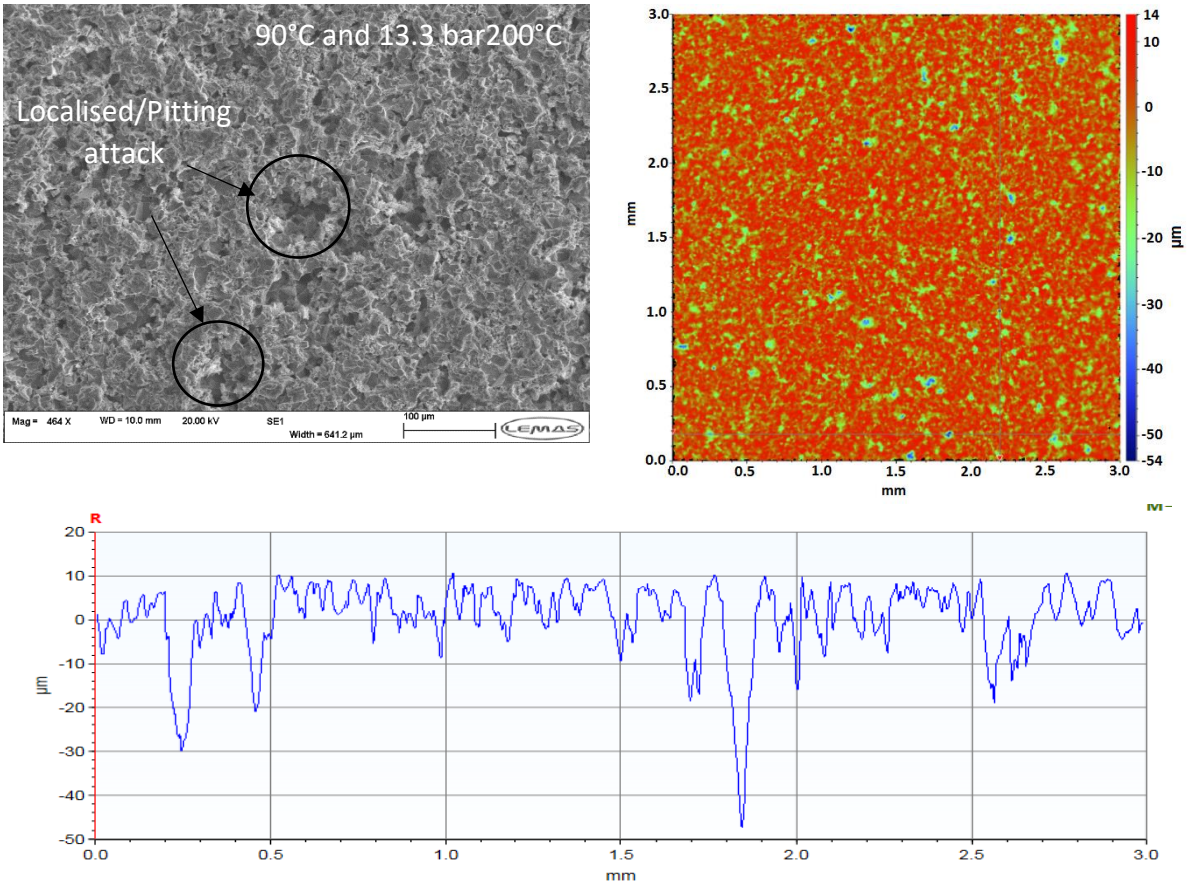
90°C and 13.3 bar200°C
Localised/Pitting attack
Mag = 464 X WD = 10.0 mm 20.00 kV SE1 100 µm Width = 641.2 µm
mm
µm
R
mm

(a)

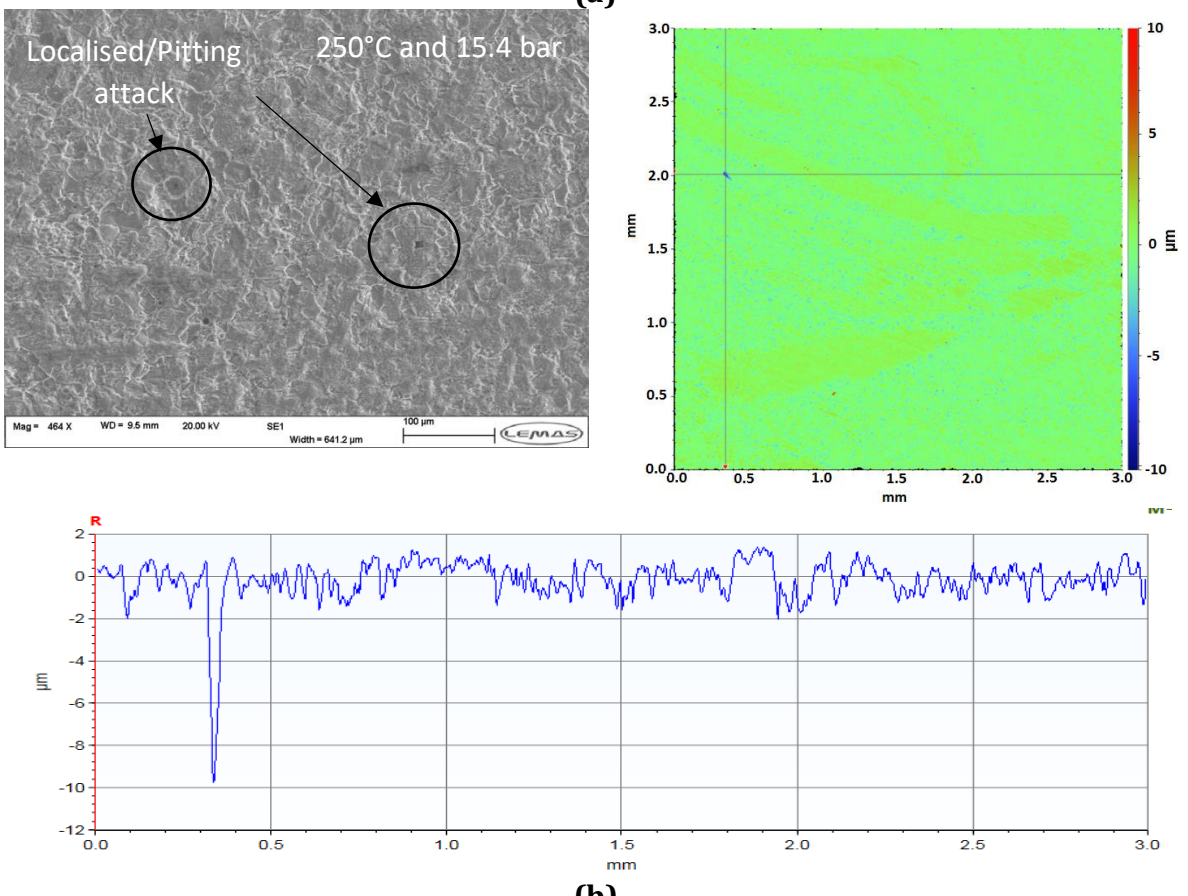
Localised/Pitting attack
250°C and 15.4 bar
Mag = 464 X WD = 9.5 mm 20.00 kV SE1 100 µm Width = 641.2 µm
mm
µm
R
mm

(b)

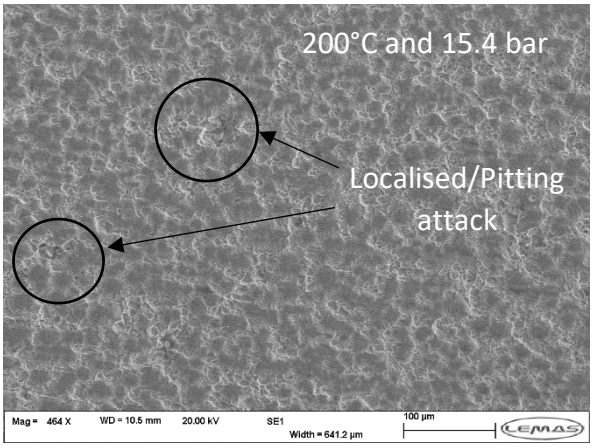
200°C and 15.4 bar
Localised/Pitting attack
Mag = 464 X
WD = 10.5 mm
20.00 kV
SE1
Width = 641.2 µm
100 µm
LEMAS

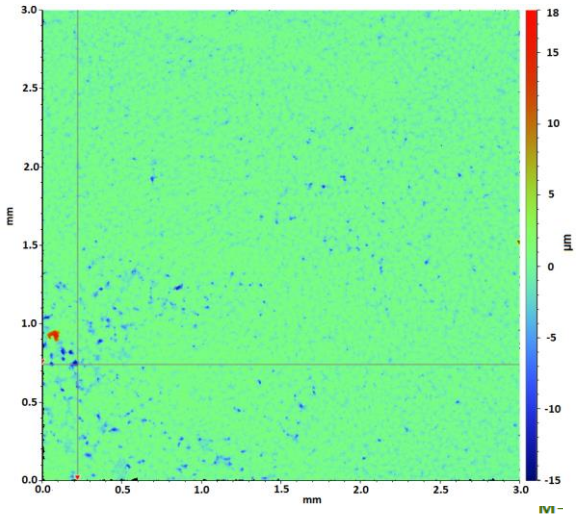
mm
µm
mm

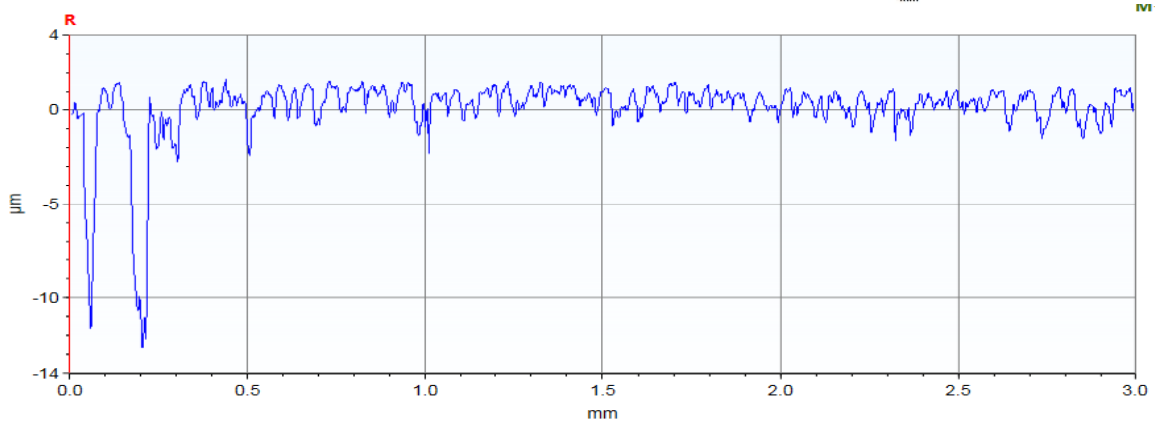
R
µm
mm

(c)

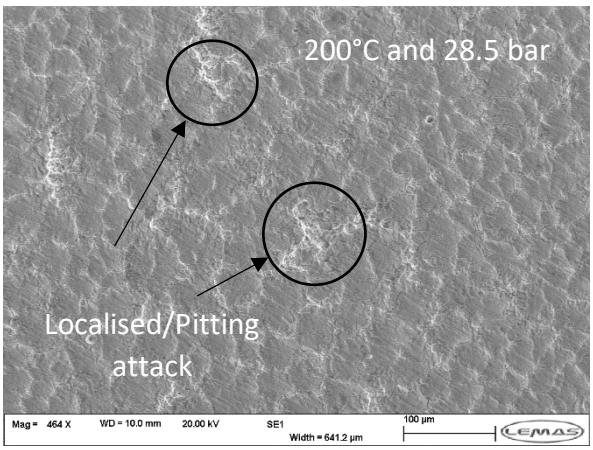
200°C and 28.5 bar
Localised/Pitting attack
Mag = 464 X
WD = 10.0 mm
20.00 kV
SE1
Width = 641.2 µm
100 µm
LEMAS

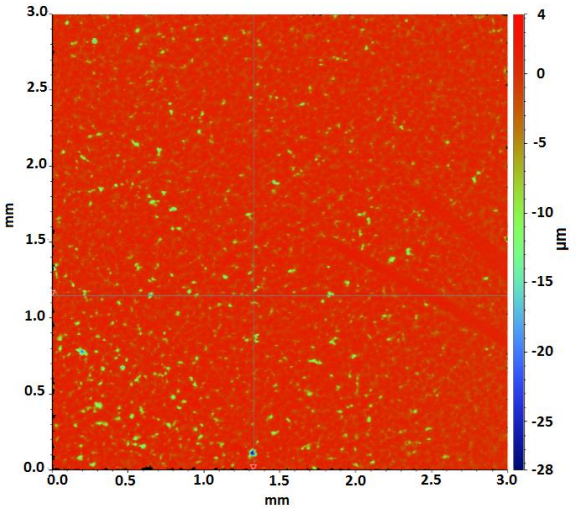
mm
µm
mm

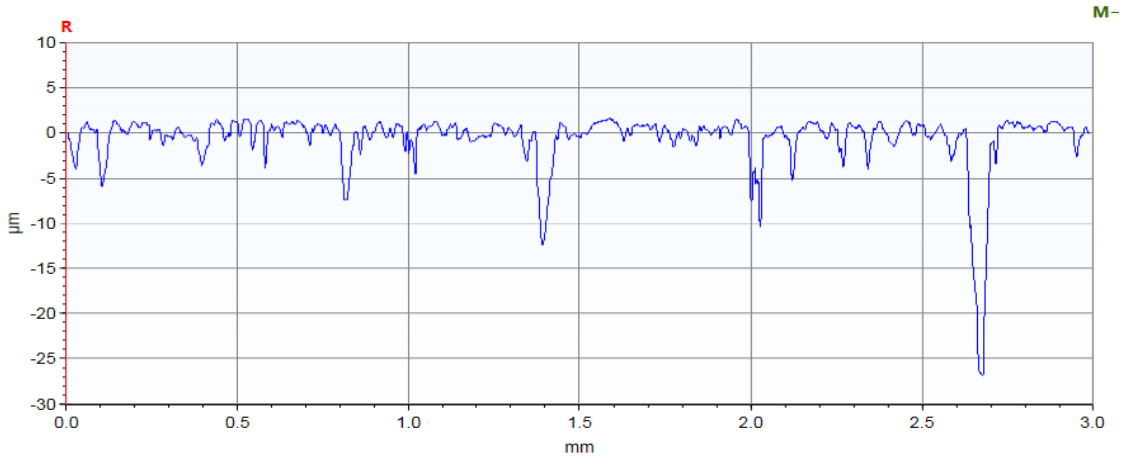

(d)

Figure 9: Examples of profilometry and SEM images of the localised/pitting attack identified after removal of corrosion products on X65 carbon steel surfaces at various temperatures and CO_2 partial pressures of (a) 13.3 bar at 90°C, (b) 15.4 bar at 250°C, (c) 15.4 bar at 200°C and (d) 28.5 bar at 200°C.

3.6 Isolating the role of temperature

One aspect which is not fully clear from the previous tests is the role of solely temperature on the formation of Fe_3O_4 and how this influences the ratio of $FeCO_3/Fe_3O_4$ on the steel surface. To provide some indication as to the individual effect of temperature, the role is considered here through an additional experiment at 250°C with the pH maintained at 4.92 and a similar partial pressure to the test conducted at 90°C earlier (13.3 bar).

The result from the additional test in comparison to the previous experiment at 90°C is shown in Figure 10. Increasing temperature from 90 to 250°C whilst maintaining pH at ~4.9 results in a reduction in corrosion rate from 3.2 to 0.9 mm/year. However, this not as substantial a reduction as when pH is increased from 4.9 to 6.3 at 250°C, where the corrosion rate was reduced to 0.3 mm/year. The SEM images in Figure 10 show that solely increasing temperature also reduces the amount of $FeCO_3$ on the steel surface and promotes Fe_3O_4 (validated by XRD), in agreement with the findings of Tanupabrungsun et al.[18] through the development of their Pourbaix diagrams. Furthermore, comparing Figure 10(b) with Figure 3(d), it can also be seen that increasing pH at constant temperature of 250°C favours Fe_3O_4 formation and supressed the precipitation of $FeCO_3$.

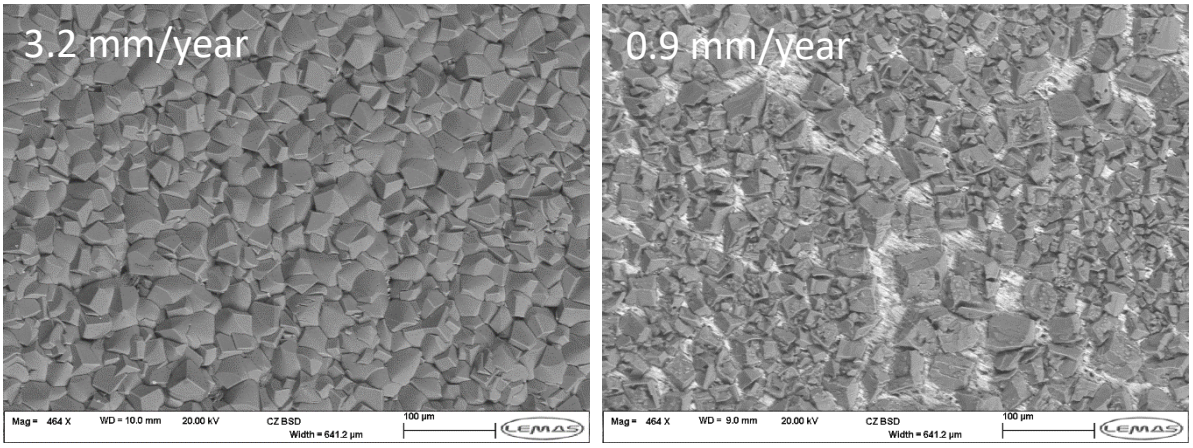

Figure 10: SEM images of the corrosion products formed on X65 carbon steel surfaces after 48 hour exposure to a CO_2-saturated 4.9 wt.% NaCl brine at pH 4.9 and temperature of (a) 90°C and (b) 250°C

3.7 Isolating the role of CO_2 partial pressure

A similar analysis to that with temperature can be made to show the role of solely CO_2 partial pressure changes on the formation of $FeCO_3$ and Fe_3O_4. Additional experiments at 200°C with the pH maintained at 5.4 and CO_2 partial pressures of 2.7 and 28.5 bar are performed in this section. The general corrosion rate behaviour of X65 are shown in Figure 11 in conjunction with SEM images of each steel surface. Interestingly, the significant increase in CO_2 partial pressure has little effect on the general corrosion rate, increasing it from 0.3 to 0.4 mm/year. However, comparison of the SEM images in Figure 11 shows that there is a change in the proportion of $FeCO_3$ on the steel surface as a result of the partial pressure increase i.e. increasing partial pressure increases the quantity of $FeCO_3$ on the steel surface.

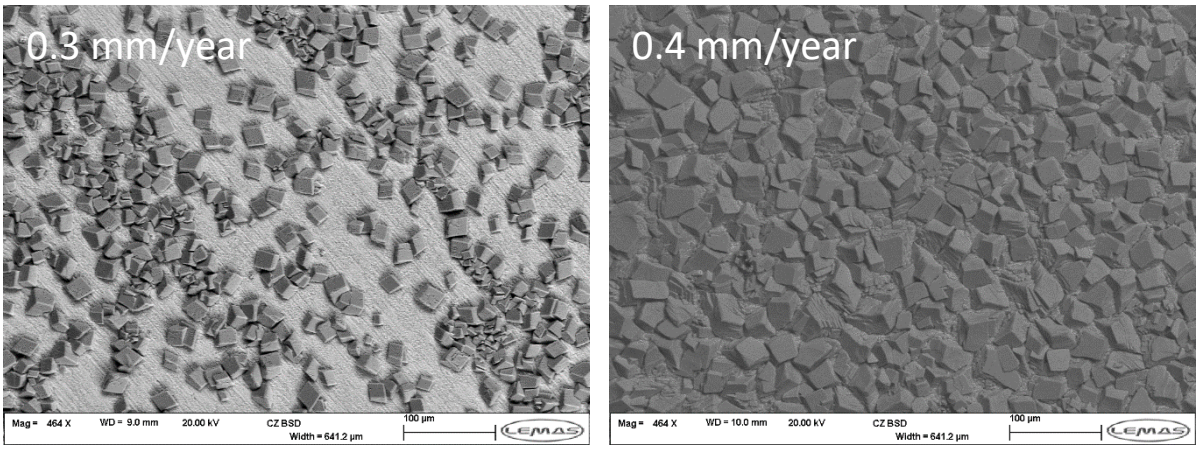

Figure 11: SEM images of the corrosion products formed on X65 carbon steel surfaces after 48 hour exposure to a CO_2-saturated 4.9 wt.% NaCl brine at pH 5.4 and 200°C with CO_2 partial pressures of (a) 2.7 bar and (b) 28.5 bar

3.8 Further analysis of $FeCO_3$ and Fe_3O_4 formation on X65 steel surface at 200°C

To further understand the chemistry of the corrosion product layer developed on the steel surface at 200°C (the experiment which produced the lowest general corrosion rate), a combination of Raman spectroscopy and FIB-SEM/TEM was employed. The use of Raman spectroscopy enabled the determination of the corrosion product film locally on the X65 steel surface. The spectra provided in Figure 12 relate to two scans conducted at the surface; one on a large cubic crystal as shown in Region A and one within Region B. The spectrum for Region A shows two main peaks located at 290 and 1086 cm^{-1}, confirming the crystals as $FeCO_3$. The two main peaks within the spectrum for Region B located at 543 and 668 cm^{-1} confirms the presence of Fe_3O_4 between the $FeCO_3$ crystals. It is this layer of Fe_3O_4 which appears to be largely responsible for the increased general and localised corrosion resistance of X65 under these conditions, given its dominance as a surface coverage when compared to the $FeCO_3$ crystals.

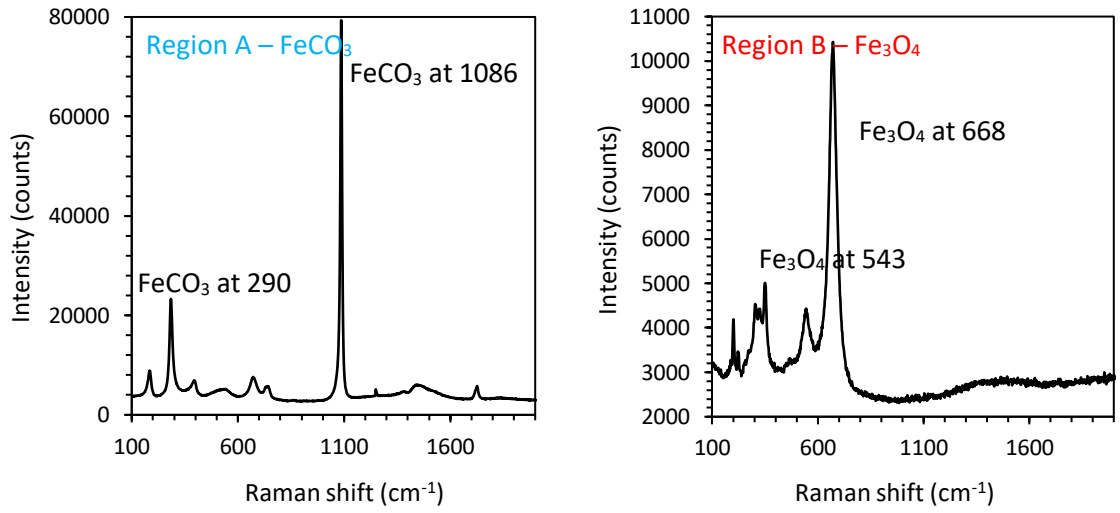

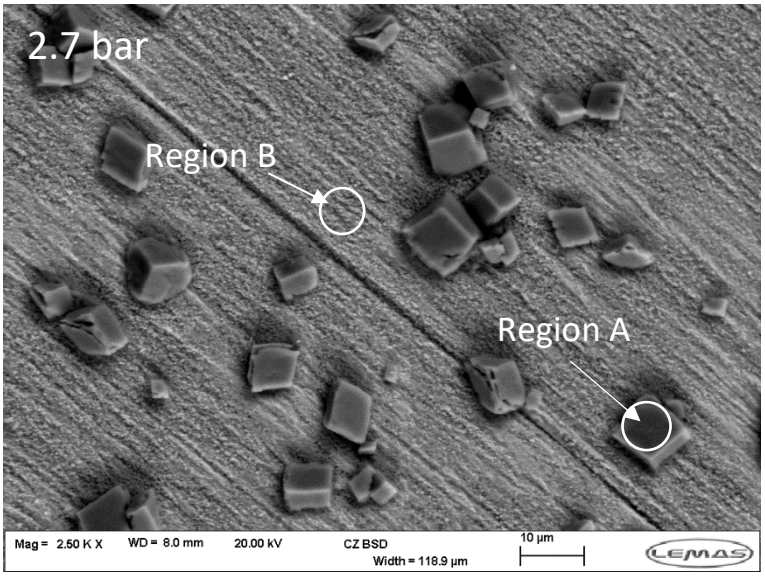

379

380 **Figure 12: Raman spectra of the corrosion products formed on X65 surface at**
381 **200°C for 48 hours and a CO_2-saturated 4.9 wt.% NaCl solution at 2.7 bar CO_2**
382 **partial pressure; Region A is a scan of an $FeCO_3$ crystals, whilst Region B is a scan**
383 **of a fine crystalline Fe_3O_4 layer.**

384

385 ***3.7 FIB-SEM and TEM analysis***

386 To complement the Raman spectroscopy analysis, FIB-SEM/TEM was used to further
387 characterise the corrosion product formed between $FeCO_3$ crystal and substrate. The
388 sample exposed to 200°C and 2.7 bar of CO_2 partial pressure for 48 hours was selected
389 and two locations covered with different corrosion products were selected, as shown in
390 Figure 13.

391 Figures 13(a) and (c) shows SEM images of the two selected areas of the sample surface.
392 The FIB samples prepared from each of these two regions were attached to Cu TEM grids
393 (Figure 13(b) and (d)). The FIB-SEM image in Figure 13(b) shows that the interface
394 between the $FeCO_3$ crystal and the steel substrate is separated by a thin interfacial layer
395 (approximately 200 nm thick). Based on the analysis of the cross-section from Figure
396 13(d), the thin layer is present across the entire steel surface as well as below the $FeCO_3$
397 crystals. Therefore, the low general corrosion observed under these conditions can be
398 attributed this thin layer (identified through Raman analysis as Fe_3O_4).

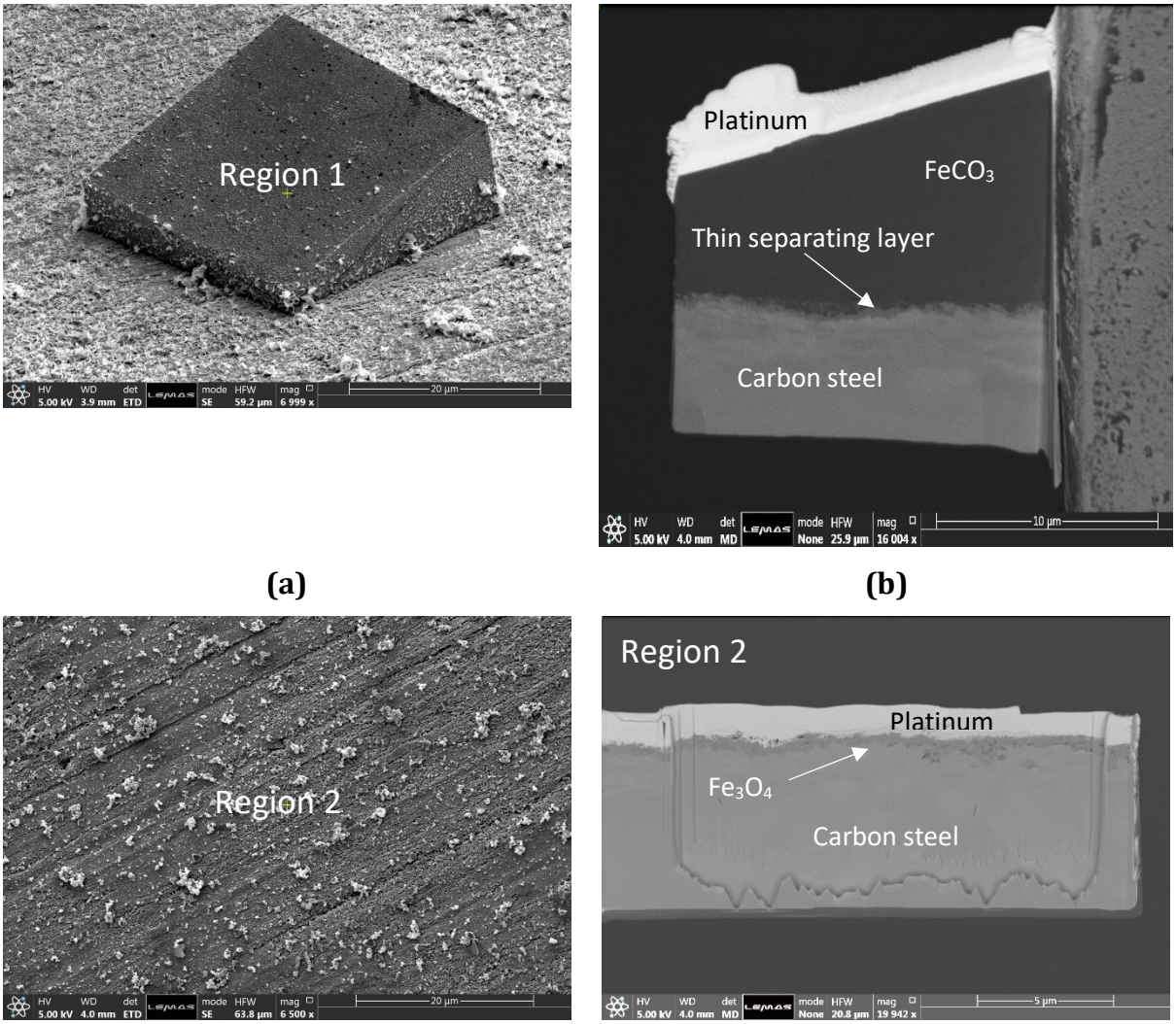

Figure 13: SEM images and FIB prepared cross-sections of two regions on the surface of X65 carbon steel exposed to a CO_2-saturated 4.9 wt.% NaCl solution at 200°C for 48 hours with a CO_2 partial pressure of 2.7 bar.

Further analysis of the interlayer between the $FeCO_3$ crystal and the substrate depicted in Figure 13(b) was performed using selected area electron diffraction. Figure 14(a) provides a higher magnification TEM image of the sample shown in Figure 13(b). Figures 14(b), (c) and (d) indicate the local electron diffraction patterns from different areas across the sample. Based on the analysis of the diffraction patterns, the interlayer is shown to comprise crystalline and nano-polycrystalline Fe_3O_4.

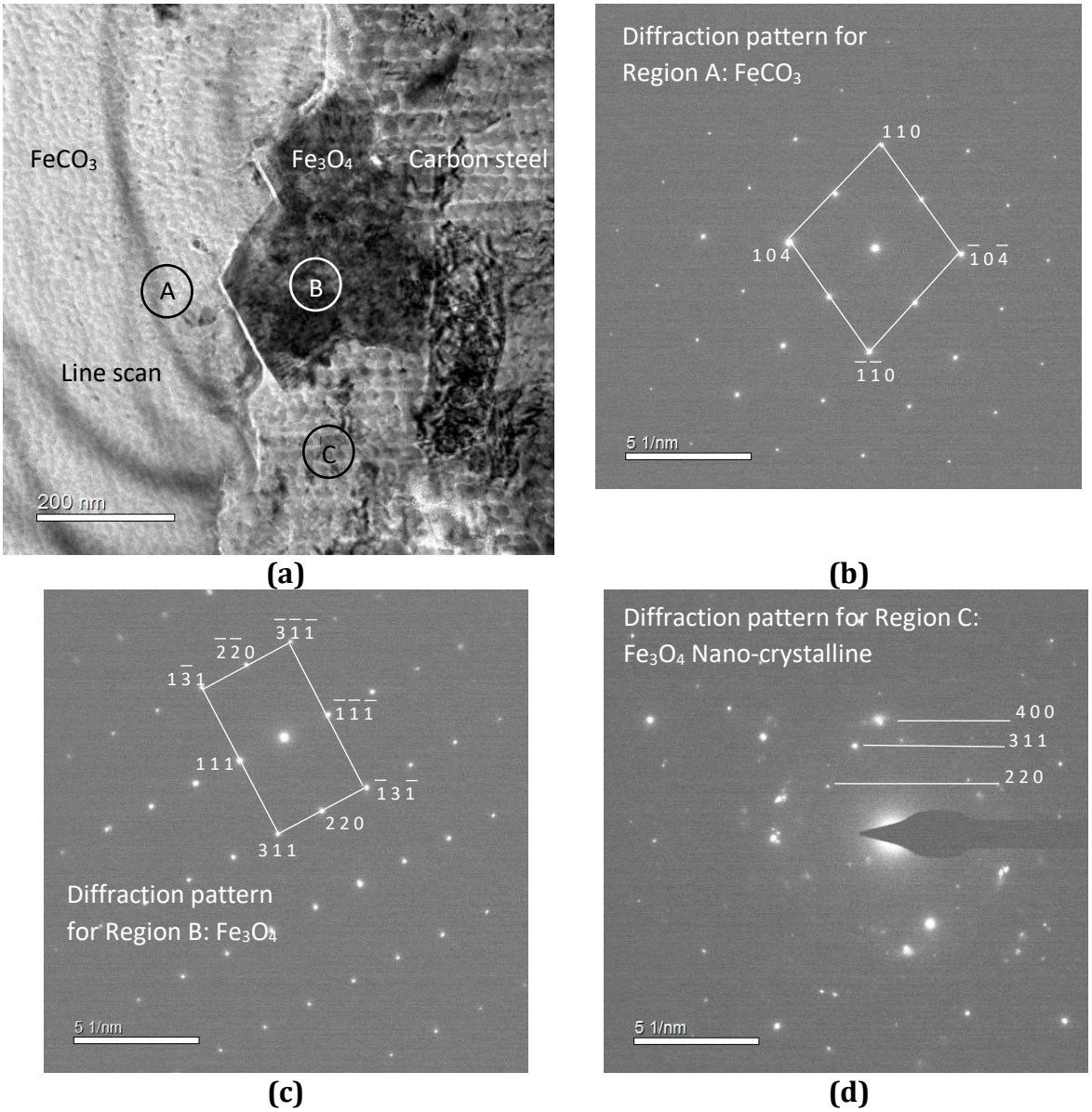

Figure 14: (a) TEM image of corrosion product in Figure 10(b), identifying regions where selected area electron diffraction patterns were collected; (b)/(c)/(d) selected area electron diffraction patterns corresponding to Regions A, B and C, respectively.

Figure 15(a) provided a higher magnification TEM image of corrosion product imaged in Figure 13(d). Indexing of the diffraction patterns produced from the thin corrosion layer observed on the sample surface (Figure 15(b)) produced d-spacing values characteristic of Fe_3O_4. The EDX line scan analysis in Figure 15(c) corroborates with the diffraction patterns collected from the TEM in that only Fe and O can be identified from the corrosion product layer and have an atomic ratio with one another which bears a strong resemblance to Fe_3O_4.

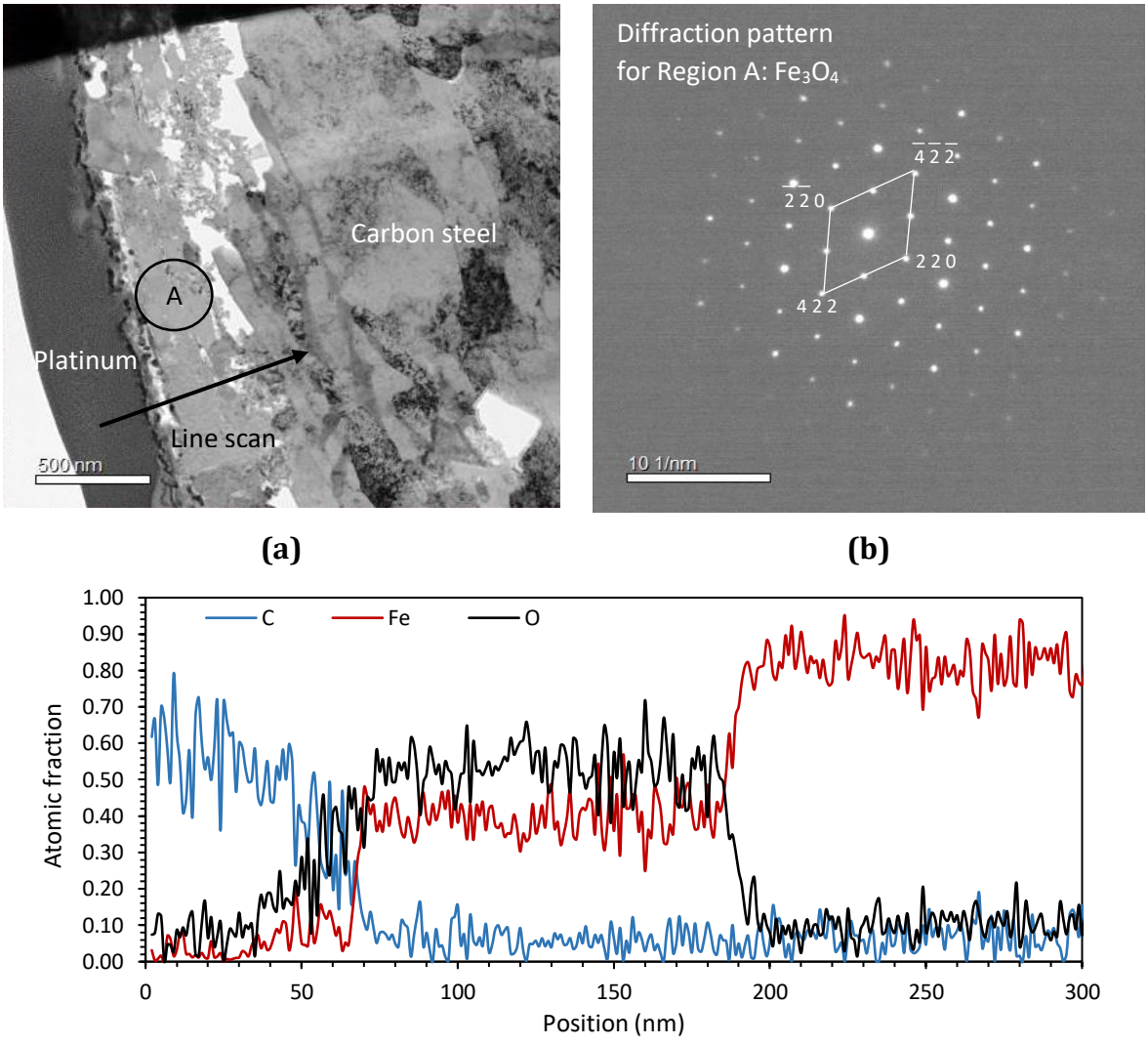

Figure 15: (a) TEM image of corrosion product in Figure 10(d), identifying the region where the selected area electron diffraction pattern and the EDX line scan were collected; (b) selected area electron diffraction pattern corresponding to region A; (c) EDX line scan result through the substrate and corrosion product layer.

4.0 Discussion

4.1 Proposed film formation mechanism

Referring to the literature, it is well known that in a CO_2 environment, the solution pH at the steel-electrolyte interface can be significantly higher than that of the bulk solution[32]. This is as a result of the flux of Fe^{2+} from the steel surface and the consumption of H^+ as a result of the cathodic hydrogen evolution reaction at the steel surface[17]. According to measurements by Han et al.[32] for a bulk solution at pH 4, the surface pH was recorded as being approximately 6. However, as the bulk pH increased to 6.6, the discrepancy between the bulk and surface pH significantly reduced. A surface pH of ~6.9 was

measured under these conditions (determined through the application of a mesh capped pH probe).

In the experiment performed within this study at 200°C and CO_2 partial pressure of 2.7 bar, the bulk solution pH was calculated at ~6.4. Although the surface pH will be higher than this, based on the measurements performed by Han et al.[32], the anticipated surface pH will be higher than this. Furthermore, the significant suppression of corrosion rate as a result of the $Fe_3O_4/FeCO_3$ film minimises the surface flux of Fe^{2+} from the steel surface, as well as the consumption of H^+. This means that their effect on the local pH is also minimised once the protective layer becomes established, reducing the discrepancy between bulk and surface pH.

In view of the TEM images and the SEM images at 200°C, it is suggested that the higher local pH at the steel–electrolyte interface results in the formation of the thin Fe_3O_4 layer via Reaction (5) and (6) (noting that these reactions produce H^+ ions, potentially acidifying the interface during formation):

$$3FeCO_3 + H_2O_{(aq)} \rightarrow Fe_3O_{4(s)} + 3CO_{2(g)} + 2H^+_{(aq)} + 2e^- \quad (5)$$

$$3Fe^{2+} + 4H_2O_{(aq)} \rightarrow Fe_3O_{4(s)} + 8H^+_{(aq)} + 2e^- \quad (6)$$

The reaction is followed by a decline in interfacial pH (due to the reduction in corrosion rate and also potentially the production of H^+ as a result of Fe_3O_4 formation).

In terms of other experiments performed in this study, as the operating conditions change, the thermodynamic stability and the kinetics of Fe_3O_4 and $FeCO_3$ evolves with the operating conditions. Consequently, the corrosion product which dominates the surface clearly depends on their relative thermodynamic stability in the environment, but also the kinetics of formation of each corrosion product (which is governed by temperature and CO_2 partial pressure).

4.2 Isolating the role of temperature

Figure 10 illustrates the effect of temperature on the formation of corrosion products more clearly between 90 and 250°C for a constant CO_2 partial pressure of 10 bar at 25°C. At a temperature of 90°C, the stable state of corrosion product is $FeCO_3$. As temperature is increased to 250°C, Fe_3O_4 becomes thermodynamically more stable relative to $FeCO_3$.

Based on Figure 8 and Figure 9, a reduction in general and localised corrosion rates is recorded as the temperature increases which can be related to the protective capability of the corrosion products ($FeCO_3$ or Fe_3O_4) formed on the steel surface. Numerous authors report that $FeCO_3$ is able to block active sites on the steel surface as well as acting as a diffusion barrier to electrochemically active species.[4, 13, 14] However, the lowest corrosion rate was observed at 250°C when only trace amounts of $FeCO_3$ were apparent on the steel surface and Fe_3O_4 was present in detectable levels using XRD. The results suggest that the formation of Fe_3O_4 appears to be more effective at reducing the susceptibility of the surface to general (and localised corrosion for that matter) as opposed to the crystalline $FeCO_3$ layer.

4.3 Isolating the role of CO_2 partial pressure

Similar observations in terms of the reduced general and localised corrosion rates as well as the corrosion product coverage on the surface were observed as CO_2 partial pressure decreased from 28.5 bar to 2.7 bar. Figure 11 illustrates the effect of CO_2 partial pressure on the formation of corrosion products between 2.7 and 28.5 bar for a constant temperature of 200°C. The increase in CO_2 partial pressure appears to make the formation of $FeCO_3$ more favourable relative to Fe_3O_4 on the surface. The observations suggest that the increased coverage of $FeCO_3$ was attributed to the increased CO_2 partial pressure and that the formation of Fe_3O_4 appears to be more effective at reducing the susceptibility of the surface to general and localised corrosion.

5. Conclusions

The corrosion behaviour of X65 carbon steel in CO_2-saturated brine was studied at temperatures from 90°C to 250°C and CO_2 partial pressures between 2.7 bar and 28.5 bar in experiments of 48 hour duration. From this study, the following conclusions can be made:

A very dense and compact $FeCO_3$ crystalline layer was detected at 90°C and the corrosion products were mainly comprised of $FeCO_3$ and Fe_3O_4 at 250°C. Localised corrosion was also shown to reduce with increasing temperature.

The lower CO_2 pressures favoured the formation of Fe_3O_4, while higher CO_2 pressures favoured the transition to the $FeCO_3$ phase.

The superior corrosion resistance at lower CO_2 pressures and high temperatures was attributed to the thin Fe_3O_4 layer.

Increasing temperature and pH promoted Fe_3O_4 formation, while the increased precipitation of $FeCO_3$ is observed as a result of increasing CO_2 partial pressure.

6. References:

1. T. Almeida, M.C.E. Bandeira, R.M. Moreira, and O.R. Mattos, New insights on the role of CO2 in the mechanism of carbon steel corrosion. Corrosion Science, 2017. **120**: p. 239-250.
2. T. Almeida, M. Bandeira, R. Moreira, and O. Mattos, Discussion on "Electrochemistry of CO_2 corrosion of mild steel: Effect of CO_2 on iron dissolution reaction" by A. Kahyarian, B. Brown, S. Nesic,[Corros. Sci. 129 (2017) 146–151]. Corrosion Science, 2018. **133**: p. 417-422.
3. A. Kahyarian, B. Brown, and S. Nesic, Electrochemistry of CO_2 corrosion of mild steel: Effect of CO_2 on iron dissolution reaction. Corrosion Science, 2017. **129**: p. 146-151.
4. W. Sun and S. Nesic, Basics revisited: kinetics of iron carbonate scale precipitation in CO_2 corrosion. Corrosion/2006, paper, 2006(06365).
5. F. Farelas, M. Galicia, B. Brown, S. Nesic, and H. Castaneda, Evolution of Dissolution Processes at the Interface of Carbon Steel Corroding in a CO_2 Environment Studied by EIS. Corrosion Science, 2010. **52**(2): p. 509-517.
6. Y. Hua, R. Barker, C. T, M. Ward, and A. Neville, Relating Iron Carbonate Morphology to Corrosion Characteristics for Water-Saturated Supercritical CO_2 Systems. The Journal of Supercritical Fluids, 2014. **vol. 98**: p. 183-193.
7. Y. Hua, R. Barker, and A. Neville, Effect of temperautre on the critical water content for general and localised corrosion of X65 carbon steel in the transport of supercritical CO_2. The International Journal of Greenhouse Gas Control, 2014. **31**: p. 48-60.
8. L. Wei, X.L. Pang, C. Liu, and K.W. Gao, Formation mechanism and protective property of corrosion product scale on X70 steel under supercritical CO_2 environment. Corrosion Science, 2015. **100**: p. 404-420.
9. A. Dugstad, The importance of $FeCO_3$ supersaturation on the CO_2 corrosion of mild steels. CORROSION/92, paper, 1992(14).
10. K. Gao, F. Yu, X. Pang, G. Zhang, L. Qiao, W. Chu, and M. Lu, Mechanical properties of CO_2 corrosion product scales and their relationship to corrosion rates. Corrosion Science, 2008. **50**(10): p. 2796-2803.
11. Y.C. Zhang, X.L. Pang, S.P. Qu, X. Li, and K.W. Gao, Discussion of the CO_2 corrosion mechanism between low partial pressure and supercritical condition. Corrosion Science, 2012. **59**: p. 186-197.
12. B. Ingham, M. Ko, N. Laycock, J. Burnell, P. Kappen, J. Kimpton, and D. Williams, In situ synchrotron X-ray diffraction study of scale formation during CO_2 corrosion of carbon steel in sodium and magnesium chloride solutions. Corrosion Science, 2012. **56**: p. 96-104.
13. Y. Hua, R. Barker, and A. Neville, Comparison of corrosion behaviour for X-65 carbon steel in supercritical CO_2-saturated water and water-saturated/unsaturated supercritical CO_2 The Journal of Supercritical Fluids, 2015. **97**: p. 224-237.

14. J.B. Sun, W. Liu, W. Chang, Z.H. Zhang, Z.T. Li, T. Yu, and M.X. Lu, Characteristics and formation mechanism of corrosion scales on low-chromium X65 steels in CO_2 environment. Acta Metall Sin, 2009. **45**(1): p. 84.
15. C. Palacios and J. Shadley, Characteristics of corrosion scales on steels in a CO_2-saturated NaCl brine. Corrosion, 1991. **47**(2): p. 122-127.
16. A. Ikeda, M. Ueda, and S. Mukai, CO2 Behavior of Carbon and Chromium Steels.(Retroactive Coverage). Advances in CO_2 Corrosion., 1984. **1**: p. 39-51.
17. J. Han, D. Young, H. Colijn, A. Tripathi, and S. Nešić, Chemistry and structure of the passive film on mild steel in CO_2 corrosion environments. Industrial & Engineering Chemistry Research, 2009. **48**(13): p. 6296-6302.
18. T. Tanupabrungsun, D. Young, B. Brown, and S. Nešic. Construction and verification of pourbaix diagrams for CO_2 corrosion of mild steel valid up to 250 C. in CORROSION 2012. 2012. NACE International.
19. R. De Marco, Z.-T. Jiang, B. Pejcic, and E. Poinen, An in situ synchrotron radiation grazing incidence X-ray diffraction study of carbon dioxide corrosion. Journal of The Electrochemical Society, 2005. **152**(10): p. B389-B392.
20. Z. Yin, Y. Feng, W. Zhao, Z. Bai, and G. Lin, Effect of temperature on CO_2 corrosion of carbon steel. Surface and Interface Analysis: An International Journal devoted to the development and application of techniques for the analysis of surfaces, interfaces and thin films, 2009. **41**(6): p. 517-523.
21. T. Berntsen, M. Seiersten, and T. Hemmingsen, Effect of $FeCO_3$ supersaturation and carbide exposure on the CO_2 corrosion rate of carbon steel. Corrosion, 2013. **69**(6): p. 601-613.
22. M. Gopal, S. Rajappa, and R. Zhang, Modeling the Diffusion Effects Through the Iron Carbonate Layer in the Carbon Dioxide Corrosion of Carbon Steel, in CORROSION 98, NACE International: San Diego, CA:NACE.
23. F. Pessu, R. Barker, and A. Neville, The influence of pH on localized corrosion behavior of X65 carbon steel in CO_2-saturated brines. Corrosion, 2015. **71**(12): p. 1452-1466.
24. T. Tanupabrungsun, B. Brown, and S. Nesic, Effect of pH on CO_2 corrosion of mild steel at elevated temperatures. CORROSION/2013, paper, 2013(48).
25. S. Nešic, G.T. Solvi, and J. Enerhaug, Comparison of the rotating cylinder and pipe flow tests for flow-sensitive carbon dioxide corrosion. Corrosion, 1995. **51**(10): p. 773-787.
26. S. Nesic, S. Wang, J. Cai, and Y. Xiao. Integrated CO_2 corrosion-multiphase flow model. in SPE International Symposium on Oilfield Corrosion. 2004. Society of Petroleum Engineers.
27. D. W. Shannon, Role of Chemical Components in Geothermal Brine on Corrosion, in NACE Corrosion1978.
28. MultiScale 7.1 is a commercial software package from Expro Group International Ltd, for more information see: http://multiscale.no/.
29. ASTM, Standard G1-03, Standard practice for preparing, cleaning, and evaluating corrosion test specimens. ASTM International: West Conshohocken, PA, 2003.
30. ASTM, Standard G46-94, Standard guide for examination and evaluation of pitting corrosion. ASTM International: West Conshohocken, PA, 2003.
31. OLI software V-2.2 (OLI engine+CPS module), OLI Systems Inc., Morris Plains, NJ, 2016.

581 32. J. Han, B.N. Brown, D. Young, and S. Nešić, Mesh-capped probe design for direct pH
582 measurements at an actively corroding metal surface. Journal of applied
583 electrochemistry, 2010. **40**(3): p. 683-690.

584
585

586